



2023

Tracing North Atlantic Continental Erosion Events During the Mid-Pleistocene Transition

Cecilia T. Bowe
Colby College

Follow this and additional works at: <https://digitalcommons.colby.edu/honorstheses>



Part of the [Geochemistry Commons](#)

Colby College theses are protected by copyright. They may be viewed or downloaded from this site for the purposes of research and scholarship. Reproduction or distribution for commercial purposes is prohibited without written permission of the author.

Recommended Citation

Bowe, Cecilia T., "Tracing North Atlantic Continental Erosion Events During the Mid-Pleistocene Transition" (2023). *Honors Theses*. Paper 1415.

<https://digitalcommons.colby.edu/honorstheses/1415>

This Honors Thesis (Open Access) is brought to you for free and open access by the Student Research at Digital Commons @ Colby. It has been accepted for inclusion in Honors Theses by an authorized administrator of Digital Commons @ Colby.

TRACING NORTH ATLANTIC CONTINENTAL EROSION EVENTS
DURING THE MID-PLEISTOCENE TRANSITION

Cecilia Bowe

A thesis submitted to the Faculty of the Geology Department of Colby College in fulfillment of
the requirements for Honors in Geology

Waterville, Maine

May, 2023

TRACING NORTH ATLANTIC CONTINENTAL EROSION EVENTS
DURING THE MID-PLEISTOCENE TRANSITION

Except where reference is made to the work of others, the work described in this thesis is my
own or was completed in collaboration with my advisory committee

Cecilia Bowe

Certificate of Approval



Dr. Bess Koffman

Assistant Professor of Geology

Colby College



Dr. Tasha Dunn

Associate Professor of Geology

Colby College



Dr. Alena Giesche

Visiting Assistant Professor of Geology

Colby College

Abstract:

The Mid-Pleistocene Transition (MPT), which occurred between 1.2 and 0.7 Mya, is characterized by changes in the periodicity and intensity of glacial-interglacial cycles. Early research into this event found that it was not triggered by changes in orbital forcing, but rather by internal climate processes. Previous studies have constrained a probable two-step mechanism, in which erosion of regolith under ice sheets increased glacial volumes and contributed to increased carbon sequestration in the Southern Ocean. Additional research has built on this, suggesting that increased glacial erosion of cratons surrounding the North Atlantic preceded a major weakening of the Atlantic Meridional Overturning Circulation (the "AMOC disruption") between MIS-25 and MIS-21 (~950-860 ka) (Yehudai et. al., PNAS, 2021; Kim et al. QSR, 2021). To better understand the evolution of regolith erosion in the North Atlantic, we present complementary K/Ar detrital provenance ages, ice-rafted debris (IRD) census counts, and mineralogical/textural analyses of IRD from 25 sediment samples spanning MIS 38-16 (1250-627.7 ka) from DSDP site 607 (41°00'N, 32°58'W; 3,427m). Initial data show increasingly older K/Ar ages in the detritus leading up to the AMOC disruption, thus indicating increased erosion of material from older areas of the Canadian shield. This is consistent with IRD census counts, which reveal an increase in IRD deposition during glacial intervals between MIS 30-23. Comparison of our census counts and K/Ar ages shows a correlation between provenance age and IRD accrual during this interval, supporting the removal of regolith by ice sheets, leading up to the AMOC disruption. Following the AMOC disruption, our data indicate younger detrital sources during glacials in the 100-kyr world. Through SEM analyses of IRD, this work establishes a record of changes in mineral abundances and microtextures during MIS 38-16 to better constrain the progression of erosional events across the MPT interval. This in-depth detrital chronology provides further insight into the origin of the MPT.

Acknowledgements:

I would like to thank my advisor Dr. Bess Koffman for giving me the opportunity to contribute to research throughout my time at Colby, as well as the assistance throughout my thesis-writing process. I would also like to thank Dr. Alena Giesche for her contributions to my thesis as a reader. I would like to thank my second reader, Dr. Tasha Dunn, for her additional help with the SEM and mineralogical analyses, as well. Thank you to Dr. Bill Sullivan for being a supportive advisor these past four years and for always being ready to help with the SEM. Thank you to Joohee Kim for being such a supportive summer research advisor, as well as my other mentors at Lamont-Doherty: Dr. Steve Goldstein and Dr. Sid Hemming for the opportunity to be involved with LDEO research as well as for helping me establish a thesis project. I would also like to thank Dr. Mike Kaplan and Dr. Dallas Abbott for putting together a great REU summer program, during which I was able to start on my thesis research. Thank you to Tanzhuo Liu for teaching me how to use the mass spectrometer and reduce data, as well as Leila Tarabein for showing me how to do census counts.

Table of Contents

List of Figures.....	2
List of Tables	2
Introduction.....	3
Background.....	6
2.1: The Mid-Pleistocene Transition.....	6
2.1A: The AMOC Crisis.....	7
2.2: Regolith Hypothesis.....	9
2.3: Changes in Ocean Carbon Storage.....	11
2.4: A Combined Mechanism.....	14
Methods.....	15
3.1: Selection of Core Site and Samples.....	15
3.2: Sample Sieving and Carbonate Leaching.....	16
3.3: K/Ar Analysis.....	17
3.4: IRD Counts.....	18
3.5: SEM Mineralogical and Textural Analyses.....	19
Results.....	21
4.1: K/Ar Ages.....	21
4.2: Census Counts.....	22
4.3: Mineralogy.....	24
4.4: Microtextural Analysis.....	26
Discussion.....	31
Conclusions.....	37
References.....	38

List of Figures

Figure 1 – Literature MPT Proxy Data (Tachikawa et al., 2017).....	8
Figure 2 – Marine-Terminating Ice Sheet Schematic.....	10
Figure 3 – DSDP Site 607.....	16
Figure 4 – IRD Grains (Kim et al., 2021).....	18
Figure 5 – Microtexture Appendix and Schematics.....	20
Figure 6 – DSDP site 607 Radiogenic and Stable Isotope Data.....	21
Figure 7 – IRD/Gram Box-and-Whisker Plot.....	23
Figure 8 – $\delta^{18}\text{O}$ and IRD/Gram Relationship.....	23
Figure 9 – Mineral Abundance Data.....	24
Figure 10 – Sample Quartz Grains and Microtextures.....	26
Figure 11 – Normalized Microtexture Data Over MPT.....	27
Figure 12 – Fracture Groove Box-and-Whisker Plot.....	29
Figure 13 – V-shaped Percussion Box-and-Whisker Plot.....	29
Figure 14 – Geochron Map of Maine, New Brunswick, and Quebec (Bradley, 2000).....	32

List of Tables

Table 1 – Paired T-Test Results: Mineral Abundances.....	24
Table 2 – Paired T-Test Results: Crushing and Abrasion Microtextures.....	28

I. Introduction:

One of the great mysteries in the study of past climate is the observed change in the frequency and magnitude of ice age cycles that occurred about a million years ago, without any concomitant shift in orbital forcings. This ‘Mid-Pleistocene Transition’ (MPT) (1.2–0.7 million years ago [My]) is revealed by $\delta^{18}\text{O}$ proxy records developed from benthic foraminifera, which document large-scale changes in global ice volume and deep ocean temperature (Katz et al., 2010). During the early Pleistocene, between ~2.6–1.2 My, ice ages followed a roughly 41 kyr glacial-interglacial (G-IG) cycle, characterized by relatively low ice volumes during glacial periods and gradual deglaciations (Lisiecki & Raymo, 2004; Raymo & Nisancioglu, 2003). Early Pleistocene glacial cycles were paced by obliquity, Earth’s axial tilt, an external climate forcing that fluctuates between 22.1° – 24.5° over 41 kyr cycles (Imbrie et al., 1992). When the Northern Hemisphere (NH) tilts farther away from the Sun, less solar forcing ushers in a glacial period (Imbrie et al., 1992). However, beginning at ~1.2 My, G-IG cycles began to decouple from obliquity, marking the onset of the MPT (Imbrie et al., 1992). Over this transition, glacial cycles gradually lengthened to 100 kyr, wherein the first true 100 kyr cycle occurred at ~900 kyr during the ‘900 kyr event’. This transition was completed by ~700 ka (Clark et al., 2006). During the evolution from the 41 kyr world to the 100 kyr world, $\delta^{18}\text{O}$ values document more extreme G-IG cycles, exhibiting greater temperature fluctuations and higher ice volume contrasts between glacials and interglacials (Lisiecki & Raymo, 2004). G-IG cycles following the emergence of the ‘100 kyr world’ have maintained this pattern up to the Holocene.

The onset of the MPT effected a decoupling between obliquity and G-IG cycles, for reasons still under study. Throughout the MPT, there were no significant changes in insolation, indicating that externally-forced orbital cycles cannot account for the MPT (Imbrie et al., 1992).

Rather, the MPT must have been caused by internal climate forcings, such as changes to land surfaces or greenhouse gas concentrations, for example. Subsequent research into the enigmatic origins of the MPT has generated numerous hypotheses, including decreased CO₂ concentrations and the regolith hypothesis.

According to a CO₂-driven mechanism, the MPT was caused by a decline in average glacial pCO₂ levels, which resulted in larger, longer-lived ice sheets. Beyond changes in the $\delta^{18}\text{O}$ record, the MPT is also marked by a decrease in atmospheric CO₂. While direct ice-core measurements of pCO₂ only extend back 800 ka, boron isotope reconstructions of CO₂ levels reveal a decline in average pCO₂ across the MPT (Farmer et al., 2019; Hönlisch et al., 2009). Notably, glacial pCO₂ levels were higher prior to the MPT, corresponding to ~1.06 kelvin (K) warmer glacials pre-MPT. (Hönlisch et al., 2009). Warmer pre-MPT glacial periods have also been supported by sea surface temperature (SST) reconstructions (Medina-Elizalde & Lea, 2005). Declined atmospheric pCO₂ during glacials may have led to the longer glacial cycles seen in the $\delta^{18}\text{O}$ record. However, the observed decline in atmospheric pCO₂ likely occurred due to increased ocean carbon storage, which necessitates an additional mechanism as such changes would not arise spontaneously (Qin et al., 2022).

Conversely, the regolith hypothesis proposes that a change in sub-ice sheet substrate caused the MPT. According to the 'regolith hypothesis,' regolith—the layer of unconsolidated material weathered from underlying bedrock—overlying the Canadian Shield bedrock was eroded during the 41 kyr world of the early Pleistocene, eventually exhuming bedrock. Bedrock provided more favorable conditions for the growth of higher-volume ice sheets that were more resistant to ablation, thus ushering in the longer, higher-magnitude glacials of the 100 kyr world.

Other climatic factors, such as changes in carbon cycling and ocean circulation, likely aided in this process.

Higher volume ice-sheets, which developed atop crystalline bedrock, extended to continental margins, and thus began to directly interact with the ocean. As ice sheets calved, they carried substrate eroded by glaciers into the ocean. This ice rafted debris (IRD) was deposited as the icebergs melted, leaving a record of G-IG cycles on the ocean floor. Additionally, icebergs introduced large volumes of freshwater into the ocean, slowing thermohaline circulation and increasing deep ocean carbon storage as the ocean grew more stratified (Yehudai et al., 2021; Qin et al., 2016). The effects of this increased freshwater intensified during the 900 kyr event, disturbing water mass circulation in the North Atlantic (Pena and Goldstein, 2014). Subdued thermohaline circulation and increased carbon storage decreased atmospheric $p\text{CO}_2$, cooling the climate, which supported the establishment of the 100 kyr world (Pena & Goldstein 2014; Yehudai et al., 2021). In this way, changes in $p\text{CO}_2$ likely aided in the onset of the MPT, but were not solely responsible for it.

Here, we supplement existing $\delta^{18}\text{O}$, $\delta^{13}\text{C}$, and ϵNd records with K/Ar records, IRD census counts, mineralogical evaluations, and quartz microtexture analyses developed from North Atlantic sediments from DSDP site 607 (41°00' N, 32°58' W; 3,427 m). K/Ar dating of fine fraction sediment reveals the ages and provenance of eroded material deposited throughout the MPT. This provenance approach provides an additional way to test the regolith hypothesis. Moreover, it illustrates the relationship between continental input and water mass chemical signatures, which are influenced by the introduction of weathered material. IRD counts and mineralogical analyses quantify the input, type, and weathering patterns of continental minerals and lithic grains deposited at site 607 by icebergs. Finally, examining and quantifying glacially-

caused quartz microtextures may reveal changes in weathering type and intensity associated with a transition to higher-volume ice sheets. We predict a regime shift in surficial continental material underlying the Laurentide Ice Sheet, as reflected in K/Ar ages and mineralogical and textural analyses around the 900 kyr event.

II. Background

2.1 The Mid-Pleistocene Transition

The MPT occurred between 1.2 and 0.7 Ma (Marine Isotope Stages [MIS] 32-17) and marked a shift away from 41 kyr G-IG cycles, ushering in longer glacials with increased ice volume, evidenced by $\delta^{18}\text{O}$ signals (fig. 1) (Lisiecki & Raymo, 2005; Raymo et al., 1997; Ruddiman et al., 1986). Stable isotope records suggest that this transition was gradual (Raymo et al., 1997). Sequential glacial cycles increased in length, reaching approximately 100 kyr at ~900 kyr, the ‘900 kyr event’ (Huybers 2011; Clark et al., 2006). Development of 100 kyr glacial cycles occurred in the absence of changes in Earth’s orbit, wherein the relationship between G-IGs and similarly paced 100 kyr eccentricity cycles have been determined coincidental, as eccentricity has a negligible effect on high-latitude insolation (Huybers 2011; Clark et al., 2006). In addition to the length and intensity of glacial periods, glacial terminations also changed during the MPT. The 41 kyr world—prior to the MPT— saw gradual deglaciations paced by obliquity. Late Pleistocene glaciations display a distinct ‘sawtooth’ pattern, arising from deglaciation occurring over ~10 ka (fig. 1). Such rapid deglaciation has been primarily attributed to ice sheet instability, wherein large, ‘marine terminating’ (ice sheets which extend to the continental shelf) ice sheets reach a terminal volume and rapidly calve, leading to deglaciation (Pollard, 1983; Watts & Hayder, 1984). Beyond lengthened, intensified G-IGs, the MPT altered North Atlantic

Ocean circulation, stalling formation of North Atlantic Deep Water (NADW) and causing northern incursions of Southern Source Water (SSW) during glacial periods (Yehudai et al., 2021; Pena and Goldstein 2014). Increased ice volume, rapid deglaciation, and suppressed NADW differentiate the extended glacials of the 100 kyr world from those of the 41 kyr world (Raymo et al., 1997; Ruddiman et al., 1986).

2.1A The AMOC Crisis

The Atlantic Meridional Overturning Circulation (AMOC), the Atlantic branch of the global thermohaline circulation, experienced significant changes leading into the 900 kyr event. During the early-to-mid Pleistocene, NADW export to SSW and Circumpolar Deep Water (CDW) masses was not affected by glaciation (Pena and Goldstein 2014; Kim et al., 2021). However, during the MPT, NADW formation varied in pace with G-IG cycles. Beginning at 900 kyr, NADW shoaled (got shallower) significantly during glacial periods, coinciding with the onset of 100 kyr G-IG cycles (Pena and Goldstein, 2014). The 900 kyr event also coincided with a complete collapse of NADW– the AMOC crisis– (Pena & Goldstein, 2014) and weakening of NADW during subsequent glacial periods. Changes in NADW emerged as a response to marine terminating ice sheets, characteristic of post-MPT G-IG cycles. Icebergs released from ice sheets consistently injected fresh water into the North Atlantic, decreasing ocean water density and stalling thermohaline circulation (Pena and Goldstein, 2014). This disruption to ocean circulation increased SSW and CDW influence, which displaced NADW in the deep North Atlantic during glacials (Kim et al., 2021; Pena and Goldstein 2014; Yehudai et al., 2021). In addition to affecting ocean circulation patterns, the AMOC disruption modified atmospheric and oceanic carbon cycling.

The MPT's cause remains an area of active research. Unlike glacial cycles in the 41 kyr world, post-MPT G-IG cycles were not paced by orbital patterns (Clark et al., 2006; Imbrie et al., 1992). Rather, the MPT likely originated from internal climate forcings and feedbacks (Clark et al., 2006; Huybers et al., 2011; Maslin et al., 1998). $\delta^{18}\text{O}$, $^{87}\text{Sr}/^{86}\text{Sr}$, and $\delta^{13}\text{C}$ records suggest changes in glacier substrate and/or lower glacial atmospheric CO_2 levels as causes of the MPT (Blum 1997; Clark & Pollard 1998; Farmer et al., 2019; Maslin et al., 1998; Qin et al., 2022). While bedrock and CO_2 were traditionally studied as individual instigators, recent research indicates they likely worked in concert to drive the MPT and initiate the 100 kyr world (Qin et al., 2022; Williet et al., 2019)

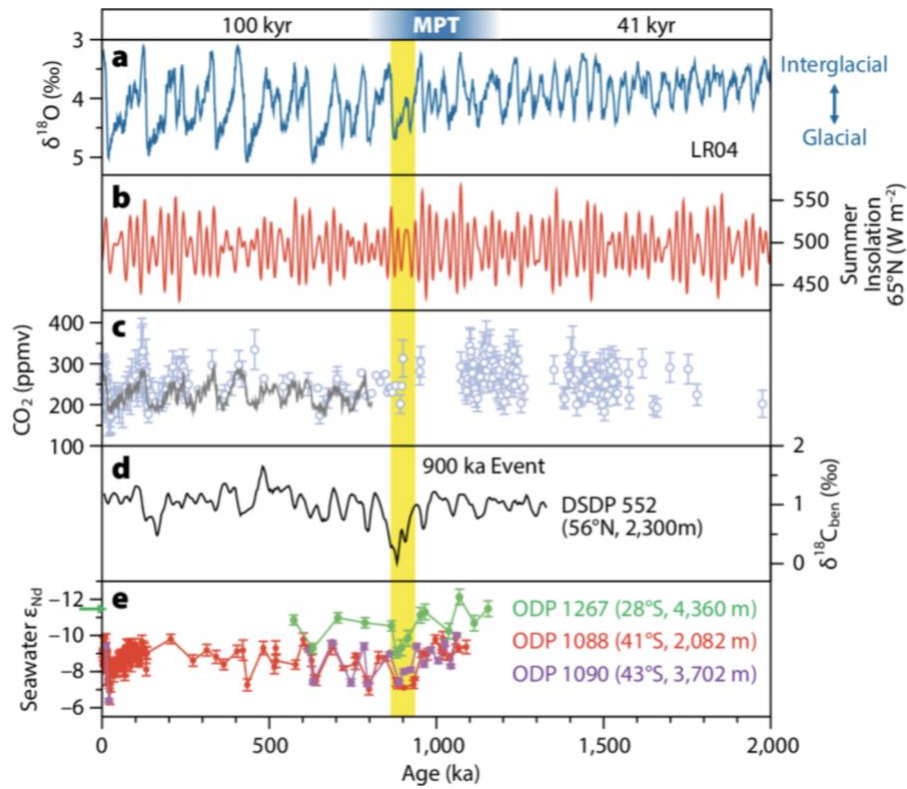


Figure 1. Figure displays MPT conditions extracted from proxies leading into and out of the 900 kyr event (yellow band). Top panel shows LR04 stack of isotopic oxygen anomalies in ocean sediment cores, representative of global ice volume and ocean temperature (Lisiecki and Raymo, 2005). More positive values are associated with higher ice volume and lower temperatures. b) Summer insolation levels, representing radiative forcing at mid-latitudes. c) CO_2 in ppm showing variable decrease during the MPT, followed by increased levels post-MPT. d) $\delta^{13}\text{C}$ [sic] (states as $\delta^{18}\text{C}$) showing sharp decrease leading into the MPT. e) seawater ϵ_{Nd} , reporting dominant water mass at each site. Higher ϵ_{Nd} corresponds with NSW and lower levels indicate SSW influence. Y-axis green arrow shows modern

seawater ϵNd (Tachikawa et al., 2017). Figure constructed by Tachikawa et al. (2017), using data from Dausmann et al. (2017); Farmer et al. (2019); Howe et al. (2016); Hu et al. (2016); and Pena and Goldstein (2014). The green arrow along the y-axis indicates the present-day seawater ϵNd value estimated by the empirical equation using temperature and dissolved oxygen concentration (Tachikawa et al., 2017).

2.2 *Regolith Hypothesis*

Changes to internal ice sheet dynamics driven by progressive erosion of regolith overlying the North American continent represent one of the leading proposed mechanisms driving the MPT. According to the hypothesis, shifts in Northern Hemisphere internal ice sheet dynamics due to substrate changes caused the MPT. Early-Mid Pleistocene glaciers (2.6-1.2 My) overlaid deformable regolith with low basal shear stress, which generated thin ice sheets (Clark & Pollard 1998; Roy et al., 2004). Pre-MPT ice sheets eroded underlying substrate over time, eventually unearthing bedrock. Once atop crystalline bedrock, Northern Hemisphere ice sheets grew larger and more resistant to climatic variations (Clark & Pollard 1998).

During this period, $\delta^{18}\text{O}$ records show a 50 m sea level equivalent increase in ice volume, sustained over a fixed areal extent, establishing substrate morphology as a primary control of ice sheet volume (Clark et al., 2006; Roy et al., 2004). Mineralogical and provenance data reveal a difference in substrate mineralogy between the early and late Pleistocene, suggesting the exhumation of fresh, Canadian Shield bedrock during the MPT (Roy et al., 2004; Clark & Pollard, 1998). This substrate erosion likely commenced during the onset of Northern Hemisphere glaciation (2.7 My), in accordance with radiogenic strontium records, and concluded prior to the 900 kyr event (Blum, 1997; Yehudai et al., 2021). Ice sheets overlying crystalline surfaces, such as the Canadian Shield, grow thicker as they are not exposed to sliding associated with the deformation of softer material (Blum, 1997; Chalk et al., 2017). Beyond low basal flow, crystalline-based glaciers in MPT models receive increased precipitation, have higher

reflectivity, and lower temperatures due to heightened slopes, all of which dampen the effects of ablation (Tabor & Poulsen, 2016). Thicker ice sheets have increased resistance to insolation, thus allowing ice to persist across multiple obliquity cycles. Rapid deglaciation in the 100 kyr world is thought to occur after ice sheets reached volume thresholds. Post-MPT marine terminating ice sheets become unstable at a critical volume, at which point they collapse and send large armadas of icebergs into the North Atlantic (fig. 2) (Watts & Hayder, 1984; Clark et al., 2017). Icebergs introduced glacially-eroded mineral-preserved in ocean sediment cores as Ice Rafted Debris (IRD)-and freshwater into the North Atlantic, changing ocean chemistry and density (Clark et al., 2017). These marine terminating ice sheets of the MPT differed from early-Pleistocene ice sheets in their ability to affect ocean circulation. Retreat of late Pleistocene ice sheets increased ocean freshwater content, disrupting density-driven circulation, critical to G-IG cycles of the MPT and 100 kyr world (Yehudai et al., 2019; Bentley et al., 2007).

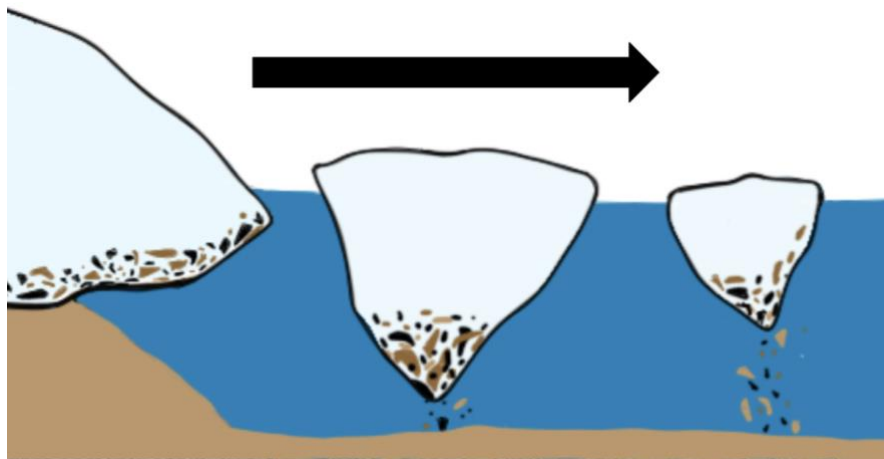


Figure 2. Schematic representation of a marine terminating ice sheet, iceberg calving, and deposition of IRD and continental sediment.

2.3 Changes in Ocean Carbon Storage

Global changes in atmospheric CO₂ may have contributed to the MPT. Boron isotope records and CO₂ numerical models show decreased ρCO_2 throughout the MPT, reflecting a change in global carbon cycling (Berger et al., 1999; Hönisch et al., 2009). This hypothesis posits that lower atmospheric CO₂ would engender a cooler climate that would in turn extend ice sheet lifespans, allowing them to surpass pacing set by 41 kyr obliquity cycles.

The observed decline in atmospheric CO₂ of 30 ppm was likely facilitated by increased deep Atlantic carbon storage and reduced Southern Ocean outgassing (Farmer et al., 2019; Lear et al., 2016). Additional changes in Atlantic carbon storage also emerge during the MPT, namely declined carbonate ion ($[\text{CO}_3^{2-}]$) saturation and increased nutrient $[\text{PO}_4^{3-}]$ concentrations (Lear et al., 2016). These geochemical signatures evince a corrosive deep Atlantic, corroborating the northern incursion of SSW (Skinner et al., 2006; Sosdian et al., 2018). The expansion of poorly ventilated SSW enhanced deep ocean carbon sequestration, which in turn lowered atmospheric CO₂ (Farmer et al., 2019; Skinner et al., 2006). Potential explanations for deep ocean CO₂ storage include iceberg-driven influxes of continental organic carbon and AMOC reorganization (Qin et al., 2022).

Raymo et al. (1997) proposed a mechanism relating regolith erosion with atmospheric carbon decline. According to their hypothesis, organic carbon stored in continental crust is exchanged with the ocean through wind and glacial-driven processes related to regolith removal. Icebergs, calved from coastal-reaching ice sheets, introduce continental material—containing organic and inorganic carbon—and freshwater to the ocean (Raymo et al., 1997). These influxes of organic carbon, once in the ocean, would undergo respiration, thus increasing dissolved inorganic carbon (DIC) and decreasing $[\text{CO}_3^{2-}]$ (Raymo et al., 1997; Qin et al., 2022).

However, reconstructions of benthic $\delta^{13}\text{C}$ indicate that changes in DIC and $[\text{CO}_3^{2-}]$ did not co-occur (Qin et al., 2022). Additionally, released continental organic carbon would undergo slight oxidation prior to its introduction into the deep ocean. This would in turn increase atmospheric CO_2 and raise temperatures, conflicting with observational evidence (Farmer et al., 2019; Qin et al., 2022). Accordingly, continental-ocean carbon exchange cannot alone account for atmospheric CO_2 levels during the MPT (Qin et al., 2022; Clark et al., 2006).

The shoaling of NADW and subsequent ocean stratification provide a more likely explanation for decreased atmospheric CO_2 . Weakened NADW, associated with stronger SSW influence in the 100 kyr world, accounts for $\sim 10 \mu\text{mol kg}^{-1}$ of increased deep ocean carbon storage (Pena & Goldstein., 2014; Farmer et al., 2019). NADW converts warm, salty Gulf Stream water into southward-returning deep water. Additionally, the formation of NADW plays an important role in cycling surficial $[\text{CO}_3^{2-}]$ into southern-flowing deep water (Sosdian et al., 2018). During and after the AMOC-crisis, expanded SSW affected North Atlantic bottom water chemistry, lowering $[\text{CO}_3^{2-}]$ and increasing DIC. This shift increased deep Atlantic Ocean carbon storage by raising the lysocline, increasing carbonate dissolution (Farmer et al., 2019; Sosdian et al., 2018; Qin et al., 2022). In addition, weakened NADW contributed to intensified ocean stratification (Farmer et al., 2019). Stratification increased the residence time of deep ocean water masses, allowing for greater carbon storage.

While a mixed stratification-circulation mechanism accounts for additional oceanic CO_2 storage and decreased $P\text{CO}_2$ throughout the MPT, it cannot explain higher-volume ice sheets on its own. CO_2 records illustrate a 30 ppm drop throughout the MPT that created a more climatically-suitable environment for extended glacial periods (Berger et al., 1999; Raymo et al., 1997). These changes to Earth's carbon cycling were instrumental in facilitating the MPT,

however they cannot account for the change in ice sheet morphology. Rather, the various patterns of the MPT necessitate a combined mechanism accounting for both changes to ocean geochemistry and ice sheet morphology (Hönisch et al., 2009; Chalk et al., 2017; Farmer et al., 2019).

2.4 A Combined Mechanism

Recent studies posit that the MPT likely resulted from coeval changes to internal ice sheet processes and ocean-atmosphere carbon cycling (Chalk et al., 2017; Tabor et al., 2016; Williet et al., 2019). This hypothesis accounts for observed MPT phenomena including ice sheet growth, atmospheric carbon reduction, and ocean circulation shifts; however, the cause of carbon drawdown has not reached a consensus (Chalk et al., 2017; Qin et al., 2022). The MPT's CO₂ decline is secondary to ice sheet substrate modifications, both regarding timing and effect on G-IG cycles, yet the extent to which the two are related remains unclear.

Chalk et al. (2017) describe atmospheric CO₂ removal as a direct response to ice sheet growth. According to their interpretations, sea level drop associated with ice volume accumulation increased atmospheric dustiness. Inorganic dust released into the Southern Ocean cycled through the “Biological Pump”, where it is converted into organic material and settled into the deep ocean (Anderson et al., 2002). Influxes of dust into the Southern Ocean would have increased the magnitude of the pump, reinforcing carbon storage and reducing atmospheric carbon (Anderson et al., 2002). There is conflicting evidence relating sea level to dust quantities, making this direct ice sheet-carbon drawdown hypothesis less likely (McGee et al., 2010; De Angelis et al., 1997; Wolff et al., 2006).

Carbon drawdown due to ocean dynamics seems well-supported, given the temporal coupling between Canadian Shield excavation, PCO_2 decline, and the AMOC crisis at ~900 kya. Strong lines of evidence for drawdown arising from ocean circulation and/or stratification pair atmospheric carbon decline with the AMOC crisis and NADW shoaling (Qin et al., 2022; Sexton and Barker, 2012; Farmer et al., 2019). A causal relationship between oceanic processes and carbon storage is thus a more feasible mechanism for decreased PCO_2 than a substrate-driven process. Increased SSW residence time may have accommodated an increased PCO_2 load, thus capturing and storing converted DIC in the deep ocean (Qin et al., 2022). Current understanding of water mass behavior during the MPT is not exhaustive, yet ocean circulation played a clear role in atmospheric carbon sequestration (Pena & Goldstein, 2014; Farmer et al., 2019). A step-wise MPT consisting of regolith removal and carbon drawdown due to ocean circulation changes can explain the key observed climate shifts associated with the MPT.

2.5 K/Ar Geochronology

Research presented here takes advantage of K/Ar geochronology, an established radiogenic isotope tracer used for geologic dating and provenance (Hemming, 2019). Crustal sediment sources adopt distinct K/Ar signatures as a product of age and thermal history, allowing these ages to double as a provenance tracer. K/Ar signatures in this study are used to infer age and source location of material eroded and transported into the North Atlantic through the MPT.

Potassium is abundant in Earth's crust, with three naturally occurring isotopes: ^{41}K , ^{40}K and ^{39}K . ^{40}K is an unstable nuclide that decays into ^{40}Ar over 1.2 billion years through electron capture. The long half-life of ^{40}K makes it an attractive geochronological tool. Additionally, argon's characteristics as a noble gas make its measurement relatively simple (White, 2015).

Daughter isotope ^{40}Ar will not form bonds within crystalline lattices, and thus can be extracted in high-temperature environments (Schaen et al., 2020). Because of this, argon isotopic abundance within sediment can be measured using mass spectrometry. Sediment aliquots and known-age GLO standards (Glaucony Geostandard— mixed glauconite and smectite grains of known age) are heated above 650°C by diode lasers, releasing argon gas (Odin, 1976). Argon gas is then collected and categorized by machine filaments according to isotopic mass (White, 2015). Collected ^{40}Ar and ^{36}Ar constrain sediment ages and correct for atmospheric argon ($^{40}\text{Ar}/^{36}\text{Ar}$). ^{40}Ar is used as a proxy for ^{40}K , wherein final ages are calculated based on known/assumed moles of K and measured sample moles of Ar^{40*} (radiogenic argon) in samples (White, 2015).

III. Methods

3.1 Selection of Core Site and Samples

We selected twenty-five samples representing 23 marine isotope stages (MIS) of the MPT interval from holes A and Z of DSDP site 607 ($41^\circ00'\text{N}$, $32^\circ58'\text{W}$; 3,427m), situated in the western flank of the Mid-Atlantic Ridge in the North Atlantic (fig. 3). Site 607 is at the southern edge of the IRD belt in the North Atlantic, removed from continental margins. This location limits input of continental material to large-scale erosional events, allowing for a clearer signal when analyzing core material. Due to its location within the core of NADW in the Atlantic basin, the core from site 607 has been analyzed extensively for stable and radiogenic isotopic tracers such as $\delta^{18}\text{O}$, $\delta^{13}\text{C}$, and ϵNd (Kim et al., 2021; Raymo et al., 1989; Ruddiman et al., 1989). These additional datasets provide a more comprehensive interpretation of data as results can be compared to the evolution of glacial cycles, ice volume, and water mass movement during the MPT interval.

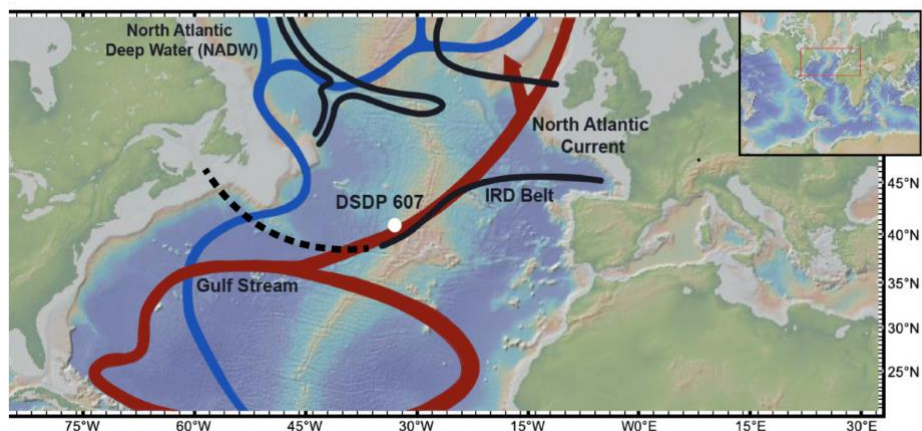


Figure 3. Map of sample location DSDP 607 and its spatial relationship to AMOC and IRD belts (Map developed using GeoMapApp).

3.2 Sample Sieving and Carbonate Leaching

We separated each sample into $>63 \mu\text{m}$ (coarse) and $<63 \mu\text{m}$ (fine) fractions using a metal sieve. Following sieving, we settled fine fraction sediments using Stokes gravity settling and poured off supernatants. Fine-fraction samples dried in an oven at $50\text{-}55^\circ\text{C}$ for ~ 48 hours. Following this, we leached carbonates from ~ 2 g aliquots of the fine fraction of each sample. Each of these aliquots was transferred into clean, labeled 50 mL centrifuge tubes. To remove carbonate, 20-30 mL of buffered 1M acetic acid was added to each sample, in a 5 mL increment to avoid vigorous reaction between the reagent and sample and subsequent overflowing of the solution (Simon et al., 2020). The samples were left uncapped in a fume hood for a few hours until the reaction no longer appeared vigorous, then were capped, disaggregated using a vortex mixer, and placed on rocking tables for 6-12 hours. After centrifuging the samples at 2400 rpm for 15 minutes, we poured off clear supernatant liquid. These steps were repeated until the sediment no longer appeared to react with the acid. The carbonate-leached samples were rinsed in a thrice repeated, two-step process. We first rinsed samples with ~ 30 mL deionized water,

disaggregated them, poured off supernatant, and then centrifuged them, increasing the speed and duration with each repetition (2400 rpm for 20 minutes, 3000 rpm for 25 minutes, 3000 rpm for 30 minutes). Finally, we transferred sample slurry into clean, labeled microcentrifuge tubes to prepare them for Ar analysis. Tubes were transferred into an oven overnight to dry the slurry into clods.

3.3 K/Ar Analysis

Once completely dry, we weighed 100-260 μg of each clod and loaded it into a clean, degassed 41-spot sediment disk. GLO standards of increasing weights were placed in the final 5 spots of the disk to act as a calibration curve during analysis. We placed the prepared disk on the stage of a single-collector mass spectrometer in the AGES lab at Lamont-Doherty Earth Observatory (LDEO). Samples and standards were heated and degassed with a diode laser to measure ^{40}Ar and ^{36}Ar . The ratio of 40:36 was corrected for atmospheric argon, and the abundance of $\text{Ar}40^*$, assumed moles of K, and decay constants determined final ages.

During the initial run, the mass spectrometer's filament broke while collecting the fourth and fifth samples, so these sample measurements were lost. The remaining samples were not degassed nor collected during this run, but were analyzed as a continuation of this first disk run once the mass spectrometer was stabilized.

A partial second disk containing the two lost samples and ten other samples was analyzed to (1) determine the ages of the samples lost due to filament failure and (2) to establish the relative error in ages due to filament malfunction. Ages extrapolated from the second disk's argon runs were within 5% of the ages determined in the first run, except for one sample with a 33% higher age measured in the second run. The calibration curves showed that the accuracy of

K/Ar ages was not severely compromised by the machine; however, an error of ~10% is assumed given the mass spectrometer's filament issues.

3.4 IRD Counts

Twelve samples from MIS 30-19, representing the interval surrounding the AMOC crisis, were selected for IRD census counts. Each sample was sieved into >150 μm fractions. The >150 μm fractions were weighed and then split into representative portions using a sample splitting machine. We split each >150 μm fraction 5 times. After five splits, we distributed the 'final split' into picking trays and examined each for IRDs under an optical microscope, recording the number of IRDs in each final split (fig. 4). IRDs/sample and IRDs/gram were calculated as follows: $\text{IRDs/Sample} = (\# \text{IRDs}/5) * (5^2)$; $\text{IRDs/gram} = (\text{IRDs/sample}) / (\text{weight of } >150 \mu\text{m sample fraction})$. Using this method, a total number of 406 IRD were analyzed among all 25 samples.



Figure 4. IRD grains from DSDP site 607 (Kim et al., 2021). Grains found in census counts include quartz, hornblende, and lithic fragments

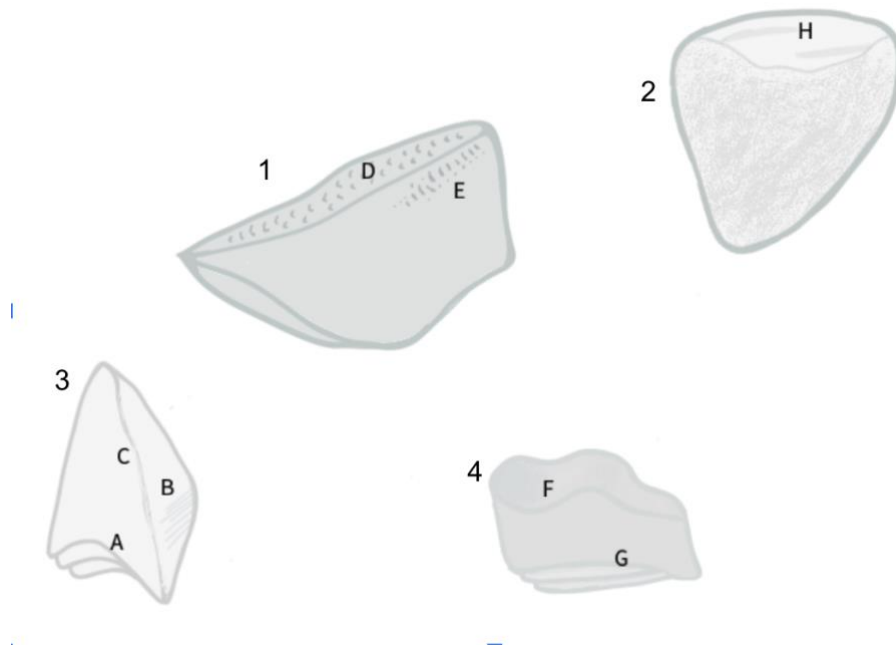
3.5 SEM Mineralogical and Textural Analyses

IRD composition and quartz-grain microtextures were determined using Colby College's Tescan Vega Scanning Electron Microscope (SEM). We worked with the same >150 μm fractions described in the previous section. We arranged each final split on trays and picked each IRD, transferring them to a carbon-tape coated aluminum stub. Once all IRDs in a sample's final split were retrieved, we prepared the IRD stubs for SEM analysis by spraying a carbon film onto each stub. Carbon coating reduces stray electron feedback, increasing the accuracy of results.

IRD stubs were placed in the center stage of the Tescan Vega SEM's main chamber. After the SEM vacuum was engaged, we moved the stage to a 15 mm working distance and activated the laser. Before examination, we ran auto gun heating on each sample to enhance image quality. We photographed each IRD grain and ran between 3–7 Energy Dispersive X-Ray (EDX) spectral analyses to determine oxides, which we then extrapolated to mineral types. Grains that showed heterogeneous compositions between spectral analyses were determined to be lithic fragments.

Following identification, images of each identified quartz grain were analyzed for nine microtextures indicative of ice sheet weathering and interaction with basal sediment/bedrock (Mahaney et al., 2002; Cowan et al., 2008). We analyzed images of each quartz grain to determine shape (angular/subangular; subround/round), relief (high/mid; low), chemical weathering (preweathered; highly weathered). Quartz grain images were also evaluated according to a series of eight microtextures representing physical glacial weathering (fig. 5). Glacial features and the corresponding glacial action (i.e. crushing vs. abrasion) were determined using indexes created by Mahaney et al. (2002). Once all glacial microtextures were recorded, we reviewed the evolution of each grain characteristic throughout the MPT, as well as changes in

crushing and abrasion. After SEM analyses, IRD were recovered and rinsed with isopropanol and ethanol to remove carbon coating.



Glacial Weathering Action	Crushing	Abrasion
	Arcuate and Straight Steps (G)	Edge Abrasion (C)
	Conchoidal Fracture (A)	V-Shaped Percussion (D)
	Subparallel Lineations (B)	Chattermark Trails (E)
	Fracture Grooves (F)	Gouges (H)

Figure 5. Cartoons of quartz grains displaying microtextures analyzed in this study. Grain 1 shows abrasive history. Grain 2 is highly chemically preweathered, save for the top face which shows abrasion. Grain 3 is angular with mixed history of crushing and abrasion. Grain 4 is angular with intensive crushing history. Individual textures are referenced in bottom table, under the weathering mechanism to which they belong.

IV. Results

4.1 K/Ar Ages

The K/Ar ages of our fine-fraction sediments ranged between ~340 and ~780 My. Comparison of these data with DSDP site 607 stable isotope records ($\delta^{18}\text{O}$ and $\delta^{13}\text{C}$) reveals a distinct pattern between glacial and interglacial intervals (fig. 6). K/Ar ages, representing the age of eroded materials' continental source, of glacially-deposited sediments increase leading into the critical period (MIS 25-21) before decreasing following the onset of the 900 kyr event. The ages of interglacial sediments show no clear trend through the MPT and remain relatively stable during and after the critical period (fig. 6).

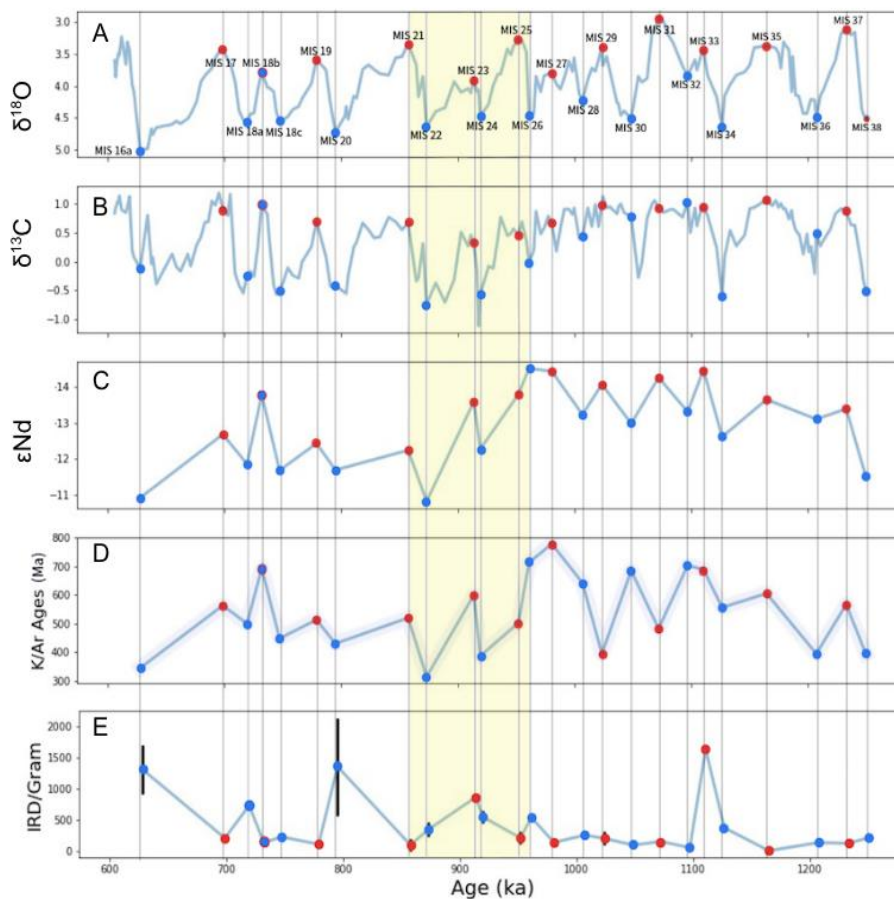


Figure 6. Stack table and radiogenic isotope data developed from site 607 between MIS 37 and MIS 16a. MIS 18b is considered a ‘lukewarm’ interglacial and as such is outlined in red. A) $\delta^{18}\text{O}$ record shows interglacial and glacial stages, which are denoted by red and blue dots, respectively (Lisiecki and Raymo, 2005). Our data (frames D & E) are presented with water mass tracers $\delta^{13}\text{C}$ (B) and ϵNd (C) (Kim et al., 2021; Ruddiman et al., 1986). D) Shows K/Ar ages analyzed from fine-fraction continental material. Ages increase during glacial periods leading into the critical period (yellow zone) suggesting a shift in the source of eroded sediment over the MPT. E) Shows IRD census counts. Error bars are present on samples with replicated census counts (MIS 16a, 20, 21, 22, 24, 25, and 29) and represent the range in measured values across two counts.

4.2 Census Counts

IRD census counts increase throughout the MPT (fig. 7). Prior to the 900 kyr event (referred to hereafter as pre-900 kyr) (MIS 38-26), IRD/gram averages 284, with an interquartile range (IQR) of 130. IRD deposition at site 607 increases significantly between the Pre-900 kyr and critical periods ($P=0.353$). During the critical period (MIS 25-21) surrounding the 900 kyr event, the average increases to 411, with an IQR of 342. Following the 900 kyr event (post-900 kyr) (MIS 20-16a), IRD/Gram averages 597 IRD/gram with an IQR of 853 (fig. 7). Notably, IRD discharge displays a moderate correlation with $\delta^{18}\text{O}$ values during glacial periods ($R^2 = 0.39$) (fig. 8). However, there is no relationship between $\delta^{18}\text{O}$ and IRD abundance during interglacials. Similarly, IRD/gram does not correlate with other available records from site 607 wherein ϵNd and K/Ar peaks occur prior to the 900 kyr event/AMOC disruption.

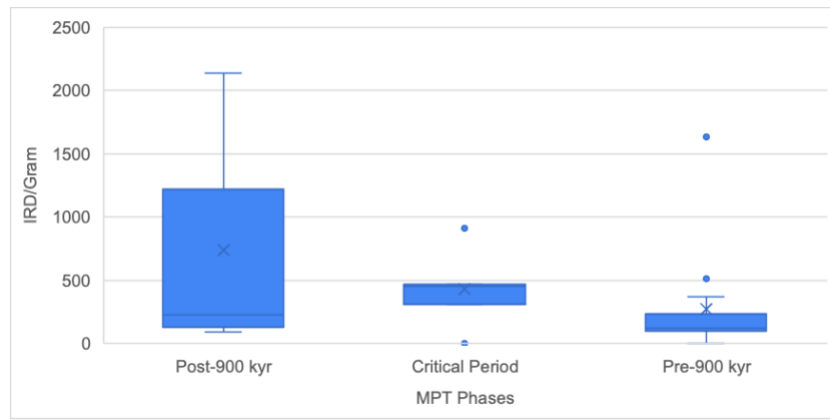


Figure 7. Data from figure 6E (IRD/Gram) displayed as box-and-whisker plots. Bins represent MIS 38-26, 25-21, and 20-16a, respectively. Outliers in pre-900 kyr phase represent MIS 26 (537) and 33 (1633). IQR is inclusive of median. N= 5140 IRD/Gram (Post-900 kyr); 2058 (critical period); 3871 (Pre-900 kyr). X indicates mean IRD/Gram and line represents median. Data show a somewhat statistically significant increase in IRD deposition at site 607 throughout the MPT ($p=0.0887$). Increase in deposition from pre-900 kyr to critical period is also somewhat significant ($p=0.0806$), while there is no significant increase following the critical period (change from critical period to post-900 kyr $p=0.4373$). IQR (represented by blue boxes) increases throughout the MPT, showing increased variability throughout the MPT.

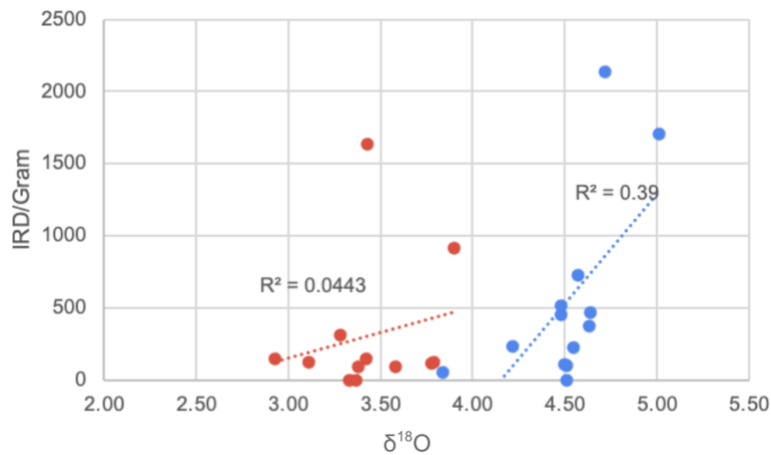


Figure 8. Relationship between $\delta^{18}O$ (6A) and IRD/gram (6E) during interglacials (red) and glacials (blue). Interglacial correlation lowered by outliers. Moderate correlation between ice volume/temperature and IRD flux during glacials may suggest higher erosion by ice sheets during these periods.

4.3 Mineralogy

Prominent mineral classes represented in our samples include quartz, micas, feldspars, and amphiboles. Lithic fragments are also common (fig. 9).

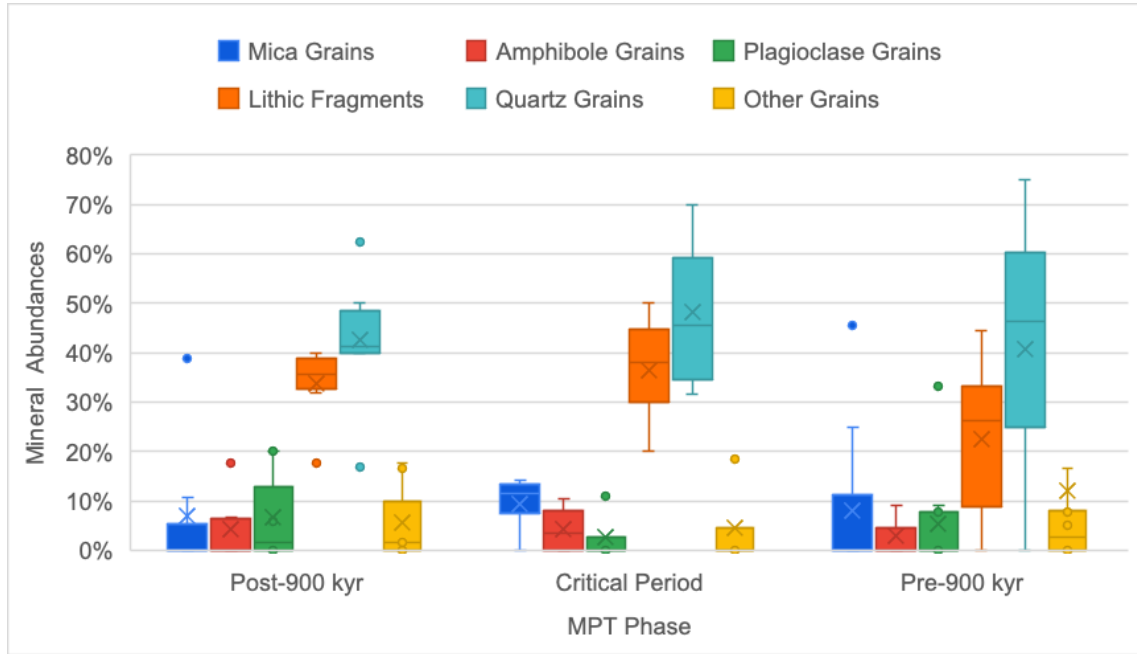


Figure 9. Mineral abundances (% of each mineral in sample) over MPT phases. Line represents mean and X represents median. IQR is inclusive of median values. **Post-900 kyr:** mica grains N=30; amphibole grains N=11; plagioclase grains N=4; lithic fragments N=54; quartz grains N=60; other grains N=7. **critical period:** mica grains N=8; amphibole grains N=5; plagioclase grains N=1; lithic fragments N=30; quartz grains N=29; other grains N=7. **Pre-900 kr:** mica grains N=17; amphibole grains N=8; plagioclase grains N=11; lithic fragments N=37; quartz grains N=85; other grains N=10. Variation in lithic grain and quartz abundance decreases over MPT phases.

Table 1. Results of two-tailed T-tests for change in mineral abundance between beginning (pre-900 kyr) and end (post-900 kyr) of MPT. No mineralogical data show significant increase or decline over the MPT.

	Mica	Amphibole	Plagioclase	Lithic	Quartz	Other
P-Value (Pre-Post 900 kyr)	0.2008	0.3055	0.9531	0.0955	0.7093	0.8402

The average abundance of quartz grains remains relatively constant throughout the MPT without any significant change (fig. 9; table 1). Quartz remains dominant within sample bulk mineralogy, peaking during the critical period, making up 48% of IRD samples on average. However, the range in quartz abundances decreases over the MPT. Pre-900 kyr event, the IQR of quartz abundance is 53%. This declines during the critical period to 34% and then to 10% following the critical period.

Lithic fragment abundance increases over the MPT (fig. 9), however, this increase is not statistically significant (table 1). During the initial phase of the MPT, lithic grains have an average abundance of 22% within samples. This increases to 37% during the critical period and decreases slightly to 34% in the post-900 kyr. The range in lithic abundance decreases over the MPT, approaching an IQR of 10% from an initial 31%, consistent with the pattern in quartz abundances. In summary, the ranges of quartz and lithic fragment abundances decline over the MPT. While both quartz and lithic fragments appear to increase in abundance over the MPT, this change is not significant.

Other, less abundant mineral classes show no significant changes throughout the MPT (fig. 9) (table 1). Mica abundance remains stable, making up an average of 9% of the bulk composition within samples. However, there are two notable exceptions. During MIS 38 and 20, mica constitutes 45% and 39% of the sample (N=5 and 23 grains, respectively). Amphibole grain abundance remains steady at ~4% across all MPT phases. Plagioclase feldspar abundance increases from 7% (pre-900 kyr) and 8% (critical period) to 20% post-900 kyr, however this increase is not significant (table 1). The ‘other grains’ category includes minerals uncommon to our samples such as apatite, alkali feldspars, and wollastonite, among others. This category’s abundance is consistent at ~5-6% throughout the MPT. Overall, IRD mineralogy remains stable

throughout the MPT. Quartz retains dominance throughout the MPT, alongside lithic grains, which show some increase between the pre-900 kyr and critical periods. Both quartz and lithic grains develop a more constrained average abundance range as the MPT progresses.

4.4 Microtextural Analysis

Our microtextural analyses of quartz grains reveal a suite of glacially-induced textures (fig. 10). While glacial-weathering processes of crushing and abrasion do not indicate significant change over the MPT, individual features such as conchoidal fractures and v-shaped percussion vary, while fracture grooves/troughs display significant evolution, indicating changes in weathering mode throughout the transition (fig. 11).

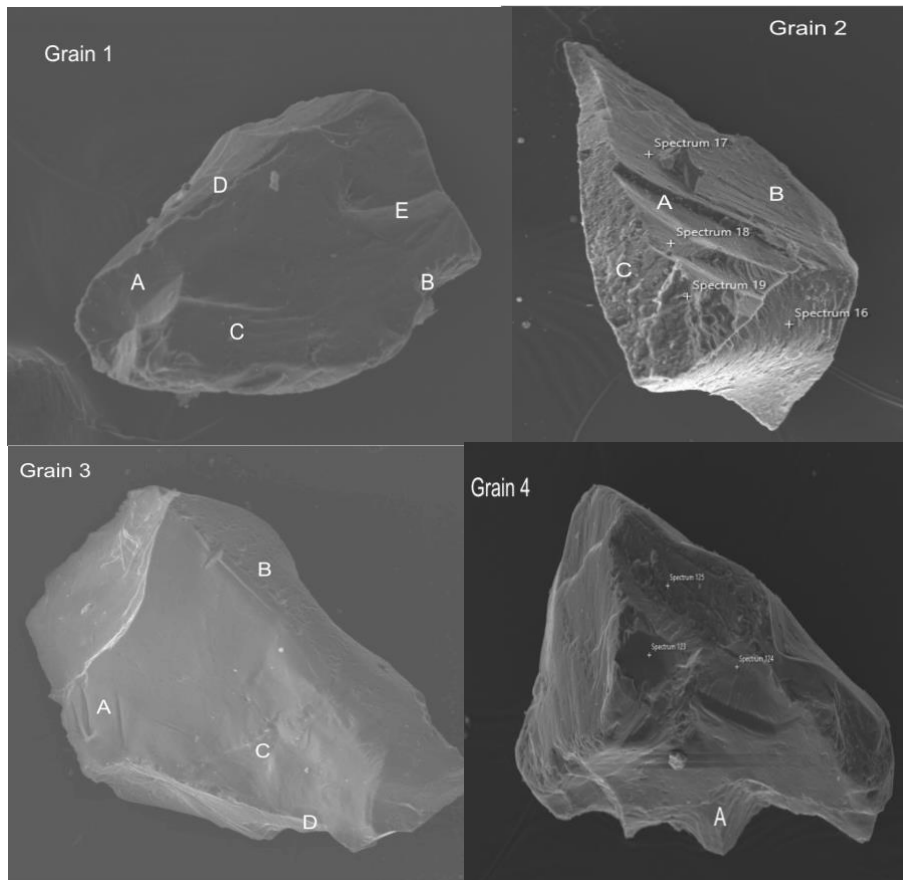


Figure 10. Examples of analyzed quartz grains. **Grain 1:** Medium relief, subangular quartz grain showing (A) conchoidal fractures, (B) arcuate steps, and (C) subparallel lineations indicative of crushing. Abrasion is also

indicated by (D) edge abrasion and (E) straight gouges. **Grain 2:** Medium relief, subangular quartz grain showing (A) conchoidal fractures, (B) arcuate steps, and (C) subparallel lineations indicative of crushing. Abrasion is also indicated by (D) edge abrasion and (E) straight gouges. **Grain 3:** Low relief, subangular grain showing (A) straight grooves, (B) V-shaped percussion, and (C) chattermark trails indicative of abrasion. (D) arcuate steps also indicate crushing. **Grain 4:** Angular, mid relief grain highlighting fracture grooves (A), a feature which emerges during the critical period.

Abrasion and crushing are shown as percentages, representing the amount of quartz grains in which microtextures indicative of each process are present. Thus, quartz grains can show one, both, or neither of these weathering actions. As all microtextures analyzed represent one of the two mechanisms, they are complementary to each other (fig. 11).

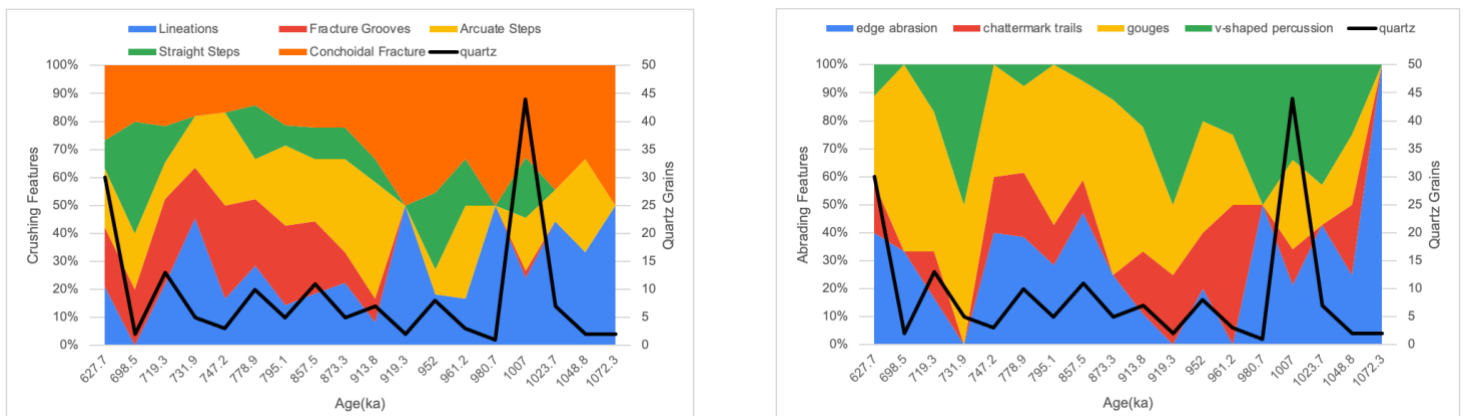


Figure 11. Normalized (100%) crushing (left) and abrading (right) features over the MPT. Samples without quartz grains (MIS 21, MIS 31, MIS 32, 35, 38) are excluded. Black line overlain shows the number of quartz grains associated with each MIS. Conchoidal fractures decrease as fracture grooves appear (left). V-shaped percussion also decreases throughout the MPT (right).

Table 2. Results of paired T-tests for change in crushing (top) and abrasion (bottom) microtextures between the beginning (pre-900 kyr) and end (post-900 kyr) of MPT. Fracture grooves display a statistically significant increase through the MPT. Lineation variation is considered statistically significant based off of a statistically significant p-value of 0.1, but fails to reject the null using a p-value of 0.05.

Texture	Lineations	Fracture Grooves	Arcuate Steps	Straight Steps	Conchoidal Fracture
P-Value (Two-Tailed T-Test)	0.0823	0.0086	0.1509	0.1651	0.9299
	Edge Abrasion	Chattermark Trails	Gouges	V-Shaped Percussion	
	0.1642	0.2371	0.0645	0.2797	

Intensive crushing, as represented by fracture grooves (sometimes referred to as troughs), emerges at the initiation of the critical period during MIS 25 (fig. 11) (Mahaney et al., 2002). The increase in fracture groove prevalence throughout the MPT is statistically significant (P=0.0086) Throughout the critical period, they represent an average of 11% of observed microtextures. This increases to 14% in the post-900 kyr phase and corresponds to a reduced IQR of 5% down from 13% (fig. 12). This suggests a more consistent presence of fracture grooves in post-900 kyr phase.

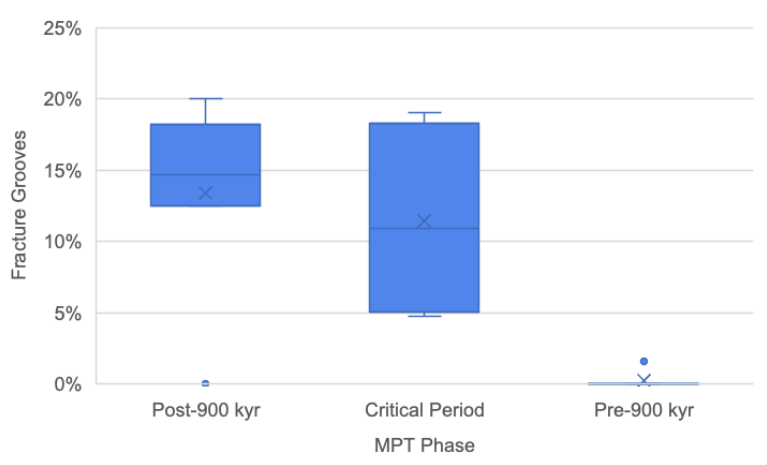


Figure 12. Fracture grooves, indicative of crushing, over the MPT. Fracture grooves outliers represent MIS 16a and 33, respectively. Fracture grooves emerge during critical period around MIS 25, coeval with decreased presence of conchoidal fractures. The increase in fracture grooves is statistically significant ($P=0.0086$).

V-shaped percussion, indicative of abrasion via turbulent meltwater, decreases from 14% to 4% between the second and first phase (fig. 13), however this decrease is not statistically significant (table 3) (Mahaney et al., 2002). The average then stabilizes to 3% during the final phase. Similarly, the IQR decreases from 17% to 8% and then 6%. As prevalence of abrasion is maintained throughout the MPT, other abrasive features, such as gouges, evolve over the MPT

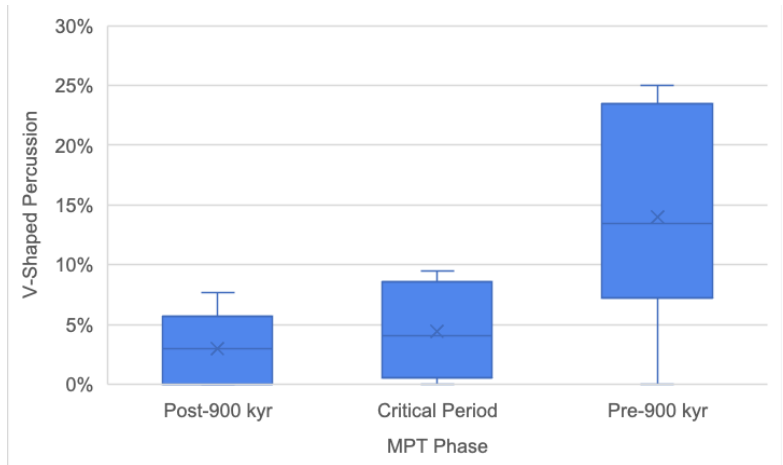


Figure 13. V-shaped percussion through the MPT. This microtexture decreases somewhat throughout the MPT, however this shift is not statistically significant based on the current sample size ($P=0.2797$).

Other analyzed grain characteristics, including relief and chemical weathering, evolve throughout the MPT, while grain shape shows no change through time. High/mid-relief quartz grains, associated with glacial action, are more common in samples than low-relief grains, peaking during the critical period, at an average of 95% (Mahaney et al., 2002). The critical period also corresponds to a reduced range in high/mid relief grains, with an IQR of 14%. Relief shows more variation on either side of the critical period. Low-relief grains peak coming out of the 900 kyr event, present in an average of 40% of quartz grains in each sample.

Quartz grains exhibiting high degrees of chemical weathering also peak during the critical period, representing an average of 60% of quartz grains in each sample. The average declines slightly post-900 kyr to 45%. Quartz grains with chemically preweathered faces increase somewhat throughout the MPT, however, this increase is not statistically significant ($p=0.1052$). The range in chemical preweathering greatly reduces during the critical period, from 32% IQR to 5%. During the final phase, the IQR increases again to 40%.

The abundance of angular and highly-chemically weathered grains peak during the critical period. Lesser chemically-weathered quartz grains somewhat increase throughout the MPT and display a small IQR during the critical period. Highly-chemically preweathered grains also somewhat increase throughout the MPT ($p=0.1060$). Grain relief also exhibits declined range during the critical period, which is also recovered in the third phase.

V. Discussion

Our K/Ar, census, IRD microtexture, and mineralogy data confirm the deposition of eroded continental material into the North Atlantic during the MPT and support the regolith hypothesis. The K/Ar analysis of fine-fraction sediment samples establishes a record of erosional

events during the MPT, highlighting erosion of different source areas through time. In the glacial intervals leading into the critical period (MIS 38-26), K/Ar ages trend older, peaking at MIS 27 (980.7 ka). These ages, ranging between ~600–780 Ma are consistent with a dominant southern Canadian Shield source, suggesting the gradual unroofing and erosion of the shield (Portier et al., 2021). As provenance reflects mixed sources, these ages could be achieved by mixing of northern Canadian Shield (800-1500 Ma) with Southern Canadian Shield (600–800 Ma) and northern Maine (350–500 Ma) sediment (Portier et al., 2021; USGS). During the critical period, K/Ar ages decrease to an average ~400 Ma, consistent with material from northern Maine and New Brunswick (350–480 Ma) as recorded by Bradley (2000); Ghanem et al. (2016); Nance & Dallmeyer (1993); and other studies compiled in USGS geochron repositories (fig. 13). Accordingly, there was likely less erosion of the newly-unroofed Canadian Shield, which is more difficult to erode, and a higher prevalence of material from northern Maine within the mixed sedimentary material. Our K/Ar data record the unroofing of the Canadian Shield prior to Portier et al. (2021), whose K/Ar ages at DSDP 625 (Gulf of Mexico) do not increase until glacials following MIS 10, significantly after the critical period and MPT.

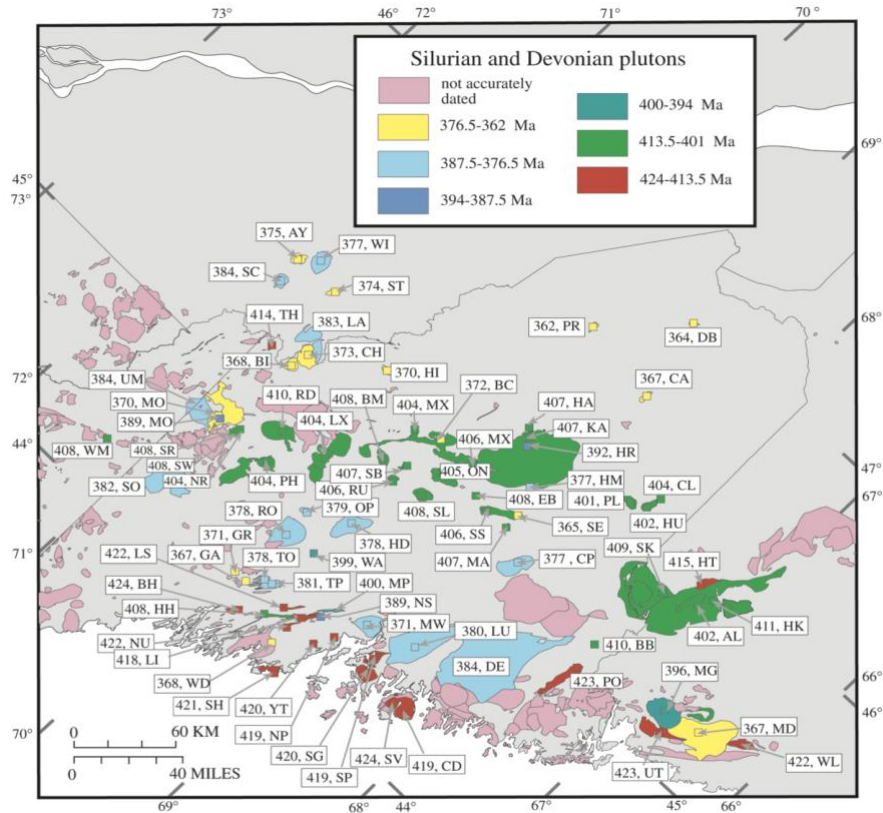


Figure 14. Geochronological ages ($^{40}\text{Ar}/^{39}\text{Ar}$ or U–Pb) of Maine, New Brunswick, and Quebec shown in boxes alongside abbreviations of plutons. Our reported K/Ar ages reflect a mixed sediment source, wherein post-critical period samples may predominantly be from Maine or New Brunswick, alongside older material from the Canadian Shield. The contribution from such older sources increases the K/Ar ages of these samples beyond what is seen in this figure.

During glacials following the AMOC-crisis, ages fluctuate but remain relatively steady at ~ 400 Ma, consistent with a source dominated by material from northern Maine and southern New Brunswick with contributions from older, Canadian sources (fig. 14) (Bradley et al., 2000, USGS). MIS 18b (731.9 ka) corresponds with the oldest sediment deposited at site 607 during this post-AMOC interval (692.5 My). While MIS 18b is unique in its characterization as a lukewarm interglacial, it follows the age trend wherein interglacials post-900 kyr tend to

correspond with older K/Ar ages than those associated with glacials (Lisiecki & Raymo, 2005). Differences in ages between glacials and interglacials is likely attributable to slightly different provenances. When ice sheets cover up large areas of land, eroded materials likely constitute a larger range of sources producing distinct, younger K/Ar ages.

Comparison of our K/Ar ages with the authigenic ϵNd record from site 607 reveals a correlation between the two that is particularly strong during glacial periods, and in all MISs following the AMOC crisis. While ϵNd records water circulation under normal conditions, the increasing influx of IRD during and after the MPT critical period overwhelms this signal. The strong correspondence between ϵNd and K/Ar age, during this period appears to reflect erosional events, especially leading into the critical period. When comparing the amount (as shown through IRD/gram) and age of material (K/Ar) deposited at site 607 with the ϵNd record, it becomes clear that the inundation of eroded material leading into and following the 900 kyr event/AMOC-disruption likely overwhelmed the signal of ϵNd as a water mass tracer during the latter half of the MPT.

During pre-900 kyr crisis glacial intervals, ϵNd records showed strong northern source water (NSW) influence. NSW is characterized by very negative ϵNd values, consistent with ancient continental material. The material deposited at site 607 during these glacials would then have very negative ϵNd values, so when paired with the amount of sediment deposited, would likely subdue the ϵNd signal coming from seawater. This interpretation is further supported by the recovery of ϵNd after the AMOC disruption. During post-900 kyr glacial periods, ϵNd reflects southern source water (SSW) incursion in the North Atlantic, which is expected due to stalling of Atlantic overturning during glacials (Pena and Goldstein, 2014). During these

intervals, the age and amount of eroded continental sediment decrease, which allows for the re-establishment of ϵNd as a water mass tracer.

Beyond elucidating the relationship between K/Ar ages and ϵNd , increasing IRD flux throughout the MPT independently supports the regolith hypothesis. Between the first phase and critical period, the average IRD/gram increases by ~ 75 . The emergence of this pattern leading into the 900 kyr/AMOC-disruption events couples them with higher rates of glacial erosion arising due to the emergence of higher-volume ice sheets. Notably, IRD deposition varies considerably in the final phase of the MPT. This range is affected by a larger difference between glacial and interglacial IRD discharge, as well as the development of quasi-Heinrich Event IRD levels after the critical period (Liu et al., 2018). Higher-volume ice sheets in the latter half of the MPT erode material more efficiently—as shown in the correlation between glacial $\delta^{18}\text{O}$ and IRD/gram—increasing the upper limits of IRD discharge (fig. 8). This accounts for the general difference in IRD deposition at site 607 during post-critical period glacial and interglacials. During the critical period, IRD levels peak during MIS 23c, coinciding with the 900 kyr event—the first true ‘100 kyr’ glacial cycle. The gradual increase in IRD flux leading into the 900 kyr event suggests a gradual-onset 100 kyr world, consistent with the findings of Raymo et al. (1997), Huybers (2011), Clark et al. (2006), and Goldstein and Pena (2014) among others. Notably, high IRD levels during the final phase of the MPT (MIS 20, 16a) reflect increased erosion by larger ice sheets and approach levels similar to more contemporary Heinrich events (Liu et al., 2018). This pattern suggests a gradual shift towards the higher erosion rate characteristic of glacials of the late Pleistocene.

While SEM-EDS measurements of IRD grains do not reflect a concrete regime shift in the bulk mineralogy of weathered material, various shifts suggest some mineralogical evolution.

Plagioclase, while sparse throughout the MPT, increases somewhat during and after the critical period. Portier et al. (2021) characterize the emergence of unweathered plagioclase at ~1My as the first signal of bedrock surfacing. While we did not calculate weathering indices for our samples, the increased abundance of plagioclase throughout the MPT may correspond to unroofing of the Canadian Shield. 'Other' and lithic grains also increase somewhat in abundance during the critical and final phases, indicating a shift towards a distinct, more diverse bulk mineralogy. Quartz and lithic fragments remain dominant throughout the MPT; however, the range in their abundances decreases post-900 kyr. This transition to a more consistent mineralogical makeup may suggest a transition to a more constrained source area during the final phase of the MPT. During the critical period, analyzed samples likely comprise a mixture of material sourced from fresh Canadian bedrock and remaining regolith, resulting in average glacial K/Ar ages of ~600 Ma. Later samples may have a more dominant Maine/New Brunswick composition as reflected in an average ~400 Ma age, which does not suggest significant input from the much older Canadian Shield (600–1500 Ma) (Portier et al., 2021). Ice streams which transport glacially-eroded material are prominent in the New England and Southern Canadian region between 40–50°N, which provides a mechanism through which such material would be deposited at site 607 (Margold, 2015). The observed mineralogical and IRD frequency shifts could also be explained by increased erosion by larger, cold-based ice sheets, as evidenced by higher $\delta^{18}\text{O}$, indicating higher ice volumes. However, the corresponding shift in K/Ar ages suggest some combination of both increased erosion and a distinct sediment source. The changes in mineralogy throughout the MPT are subtle, likely because site 607 is at the southern extent of the IRD belt and receives less continental input than more northern sites. Therefore, a more

concrete change in mineralogy through the MPT might be constrained by studying a more 'active' site of IRD deposition.

Microtextural analyses also suggest a transition to larger ice sheets. While crushing and abrasion indices remain largely the same throughout the MPT, individual microtextures and grain characteristics suggest more intensive crushing and less subglacial water flow across the MPT interval. The abundance of crushing and abrasion features remains stable throughout the transition, only briefly shifting during the critical period. During the initiation of the critical period, abrasion increases, suggesting an overall higher abrasion rate during this second phase of the MPT. Early-critical period ice sheets with more erosive capabilities than those of the early MPT may have transported high volumes of sediment relative to their overall volumes, creating higher grain-to-grain contact. Ice sheet volume and subglacial load continued to rise during the late critical period, however, rafted material may not have increased proportionally to ice sheet volume. This would account for the temporary increase in inferred grain-to-grain contact during the early critical period.

Individual microtextures such as fracture grooves also reflect the transition to larger-volume glaciers leading into the 900 kyr event. Fracture grooves emerge during the critical period and increase until stabilizing at MIS 23c. This coincides with a steady decline in conchoidal fractures, suggesting that larger ice sheets that emerged ~900 kyr realized more intensive crushing, resulting in larger crushing features. Mahaney et al. (2002) support this finding, wherein more extensive crushing is observed with larger continental ice sheets. Overall, our data support the regolith hypothesis, and suggest a gradual onset of 100 kyr periodicity.

The findings of this research also indicate areas of future investigation to better test the regolith hypothesis. Within DSDP site 607, further provenance analysis (for tracers such as

detrital ϵNd or U-Pb) would aid in constraining exact sediment sources, and thus offer further verification of source changes throughout the MPT. Detrital ϵNd , in particular, would be able to confirm whether the close relationship between detrital K/Ar and authigenic ϵNd seen during <add exact time period> is the result of increased continental erosion overwhelming the water mass signal. Additional replications of census counts, mineralogical analyses, and microtextures would also increase the validity of results and interpretations. A number of microtextural results approach statistical significance, so working with a larger data set could resolve whether such results (e.g. gouges) actually arise due to changes in eroded substrate. Finally, analyzing weathering indices on grains such as plagioclase would aid in understanding the exact timing of Canadian Shield unroofing. Beyond DSDP site 607, there have been few studies looking at provenance of eroded material during the MPT beyond Portier et al. (2021), which reports different shifts in provenance shifts associated with the MPT than those reported here (K/Ar ages of eroded material doesn't increase until MIS 10). Analyzing additional sites throughout the North Atlantic would create a more robust understanding of the MPT and the viability of the regolith hypothesis.

VI. Conclusion

The MPT has long been considered an enigmatic climate shift. Despite decades of research, uncertainty as to the event's origin and implications remain. Our multi-step approach to analyzing fine and coarse-grained sediments taken from DSDP site 607 represents the first K/Ar and microtextural analysis of MPT IRD sediments at this site, providing more details about sediment excavation, provenance, and water mass behavior surrounding the AMOC-crisis. Our K/Ar, IRD census, mineralogy, and quartz microtexture results support regolith removal as a key

mechanism underlying the MPT. Moreover, the results favor a gradual-onset of the 100 kyr event during the critical period, contrasting the findings of Pollard & Deconto (2009). This study has provided new insight on how source location, deposition rates, and erosional events evolved over the course of the MPT. This method could be applied elsewhere in the North Atlantic, the North Pacific, and the Southern Ocean to increase knowledge of ice sheet-driven erosion processes throughout the Cenozoic.

References:

- Anderson, R. F., Chase, Z., Fleisher, M. Q., & Sachs, J. (2002). The Southern Ocean's biological pump during the Last Glacial Maximum. *Deep Sea Research Part II: Topical Studies in Oceanography*, 49(9), 1909–1938.
[https://doi.org/10.1016/S0967-0645\(02\)00018-8](https://doi.org/10.1016/S0967-0645(02)00018-8)
- Bentley, C., R. Thomas, Velicogna, I. (2007) "Ice sheets" in *Global Outlook for Ice and Snow*. United Nations Environment Programme Publication ISBN: 9789280727999.
- Blum, J. D. (1997). The Effect of Late Cenozoic Glaciation and Tectonic Uplift on Silicate Weathering Rates and the Marine ⁸⁷Sr/⁸⁶Sr Record. In W. F. Ruddiman (Ed.), *Tectonic Uplift and Climate Change* (pp. 259–288). Springer US. https://doi.org/10.1007/978-1-4615-5935-1_11
- Bradley, D., Tucker, R., Lux, Harris, & McGregor, C. (2000). Migration of the Acadian Orogen and Foreland Basin across the Northern Appalachians of Maine and Adjacent Areas. USGS Professional Paper, 1624, 49.
- Chalk, T. B., Hain, M. P., Foster, G. L., Rohling, E. J., Sexton, P. F., Badger, M. P., Cherry, S. G., Hasenfratz, A. P., Haug, G. H., Jaccard, S. L., Martínez-García, A., Pälike, H., Pancost, R. D., & Wilson, P. A. (2017). Causes of ice age intensification across the Mid-Pleistocene Transition. *Proceedings of the National Academy of Sciences*, 114(50), 13114–13119. <https://doi.org/10.1073/pnas.1702143114>
- Clark, P. U., & Pollard, D. (1998). Origin of the middle pleistocene transition by ice sheet erosion of regolith. *Paleoceanography*, 13(1), 1–9. <https://doi.org/10.1029/97pa02660>
- Clark, P. U., Archer, D., Pollard, D., Blum, J. D., Rial, J. A., Brovkin, V., Mix, A. C., Pisias, N. G., & Roy, M. (2006). The middle pleistocene transition: Characteristics, mechanisms, and implications for long-term changes in atmospheric PCO₂. *Quaternary Science Reviews*, 25(23-24), 3150–3184.

<https://doi.org/10.1016/j.quascirev.2006.07.008>

Cowan, E. A., Hillenbrand, C.-D., Hassler, L. E., & Ake, M. T. (2008). Coarse-grained terrigenous sediment deposition on continental rise drifts: A record of Plio-Pleistocene glaciation on the Antarctic Peninsula. *Palaeogeography, Palaeoclimatology, Palaeoecology*, 265(3–4), 275–291.

<https://doi.org/10.1016/j.palaeo.2008.03.010>

De Angelis, M., et al. “Primary Aerosol (Sea Salt and Soil Dust) Deposited in Greenland Ice during the Last Climatic Cycle: Comparison with East Antarctic Records.” *Journal of Geophysical Research: Oceans*, vol. 102, no. C12, Nov. 1997, pp. 26681–98. *DOI.org (Crossref)*, <https://doi.org/10.1029/97JC01298>.

Ghanem, H., Kunk, M. J., Ludman, A., Bish, D. L., & Wintsch, R. P. (2016). Dating slate belts using $^{40}\text{Ar}/^{39}\text{Ar}$ geochronology and zircon ages from crosscutting plutons: A case study from east-central Maine, USA. *Journal of Structural Geology*, 93, 51–66. <https://doi.org/10.1016/j.jsg.2016.10.004>

Farmer, J. R., et al. “Deep Atlantic Ocean Carbon Storage and the Rise of 100,000-Year Glacial Cycles.” *Nature Geoscience*, vol. 12, no. 5, May 2019, pp. 355–60. *DOI.org (Crossref)*, <https://doi.org/10.1038/s41561-019-0334-6>.

Gildor, H., & Tziperman, E. (2001). A sea ice climate switch mechanism for the 100-kyr glacial cycles. *Journal of Geophysical Research: Oceans*, 106(C5), 9117–9133. <https://doi.org/10.1029/1999JC000120>

Hemming, S. R. (2019). New K/Ar age values and context from published clay mineralogy and Sr and Nd isotopes as tracers of terrigenous Atlantic Ocean sediments. *Marine Geology*, 411, 36–50.

<https://doi.org/10.1016/j.margeo.2019.01.007>

Huybers, P. (2011). *Combined obliquity and precession pacing of late pleistocene deglaciations*. Nature News. Retrieved August 10, 2022, from <https://www.nature.com/articles/nature10626>

Hönisch, B., Hemming, N. G., Archer, D., Siddall, M., & McManus, J. F. (2009). Atmospheric Carbon Dioxide Concentration Across the mid-pleistocene transition. *Science*, 324(5934), 1551–1554.

<https://doi.org/10.1126/science.1171477>

Imbrie, J., et al. “On the Structure and Origin of Major Glaciation Cycles 1. Linear Responses to Milankovitch Forcing.” *Paleoceanography*, vol. 7, no. 6, 1992, pp. 701–38. *Wiley Online Library*,

<https://doi.org/10.1029/92PA02253>.

Katz, M. E., et al. “TRADITIONAL AND EMERGING GEOCHEMICAL PROXIES IN FORAMINIFERA.” *The Journal of Foraminiferal Research*, vol. 40, no. 2, Apr. 2010, pp. 165–92. *DOI.org (Crossref)*,

<https://doi.org/10.2113/gsjfr.40.2.165>.

Kim, J., Goldstein, S. L., Pena, L. D., Jaume-Seguí, M., Knudson, K. P., Yehudai, M., & Bolge, L. (2021). North Atlantic Deep Water during pleistocene interglacials and glacials. *Quaternary Science Reviews*, 269, 107146.

<https://doi.org/10.1016/j.quascirev.2021.107146>

Liu, J., Fang, N., Wang, F., Yang, F., & Ding, X. (2018). Features of ice-rafted debris (IRD) at IODP site U1312 and their palaeoenvironmental implications during the last 2.6 Myr. *Palaeogeography, Palaeoclimatology, Palaeoecology*, 511, 364–378.

<https://doi.org/10.1016/j.palaeo.2018.09.002>

Lear, Caroline H., et al. “Breathing More Deeply: Deep Ocean Carbon Storage during the Mid-Pleistocene Climate Transition.” *Geology*, vol. 44, no. 12, Dec. 2016, pp. 1035–38. *Silverchair*, <https://doi.org/10.1130/G38636.1>.

Lisiecki, L. E., & Raymo, M. E. (2005). A Pliocene-Pleistocene stack of 57 globally distributed benthic $\delta^{18}\text{O}$ records. *Paleoceanography*, 20(1). <https://doi.org/10.1029/2004pa001071>

Mahaney, W. C. (2002). *Atlas of sand grain surface textures and applications*. Oxford University Press.

Margold, M., Stokes, C. R., & Clark, C. D. (2015). Ice streams in the Laurentide Ice Sheet: Identification, characteristics and comparison to modern ice sheets. *Earth-Science Reviews*, 143, 117–146.

<https://doi.org/10.1016/j.earscirev.2015.01.011>

- Maslin, M. A., et al. "THE CONTRIBUTION OF ORBITAL FORCING TO THE PROGRESSIVE INTENSIFICATION OF NORTHERN HEMISPHERE GLACIATION." *Quaternary Science Reviews*, vol. 17, no. 4, Jan. 1998, pp. 411–26. *ScienceDirect*, [https://doi.org/10.1016/S0277-3791\(97\)00047-4](https://doi.org/10.1016/S0277-3791(97)00047-4).
- McGee, David, et al. "Gustiness: The Driver of Glacial Dustiness?" *Quaternary Science Reviews*, vol. 29, no. 17, Aug. 2010, pp. 2340–50. *ScienceDirect*, <https://doi.org/10.1016/j.quascirev.2010.06.009>.
- Medina-Elizalde, M., & Lea, D. W. (2005). The Mid-Pleistocene Transition in the Tropical Pacific. *Science*, 310(5750), 1009–1012.
- Nance, R. D., & Dallmeyer, R. D. (1993). 40Ar/39 Ar Amphibole Ages from the Kingston Complex, New Brunswick: Evidence for Silurian-Devonian Tectonothermal Activity and Implications for the Accretion of the Avalon Composite Terrane. *The Journal of Geology*, 101(3), 375–388.
- Nyman, K. H., & Ditlevsen, P. D. (2019). The middle pleistocene transition by frequency locking and slow ramping of internal period. *Climate Dynamics*, 53(5-6), 3023–3038. <https://doi.org/10.1007/s00382-019-04679-3>
- Odin, G. S. (1976). Glauconite GL-O, interlaboratory standard for radiochronometric analysis. *Analisis*, 4(6), 287–291.
- Pena, L. D., & Goldstein, S. L. (2014). Thermohaline Circulation Crisis and impacts during the mid-pleistocene transition. *Science*, 345(6194), 318–322. <https://doi.org/10.1126/science.1249770>
- Pollard, D. (1983). A coupled climate-ice sheet model applied to the Quaternary Ice Ages. *Journal of Geophysical Research: Oceans*, 88(C12), 7705–7718. <https://doi.org/10.1029/JC088iC12p07705>
- Pollard, D., & DeConto, R. M. (2009). Modelling West Antarctic ice sheet growth and collapse through the past five million years. *Nature*, 458(7236), 329–332. <https://doi.org/10.1038/nature07809>
- Portier, A. M., Thierens, M., Martin, E. E., Hemming, S. R., Gombiner, J. H., & Raymo, M. E. (2021). Late Pleistocene Emergence of Crystalline Canadian Shield Sources in Sediments of the Northern Gulf of Mexico. *Paleoceanography and Paleoclimatology*, 36(4). <https://doi.org/10.1029/2020PA004082>

Qin, B., Jia, Q., Xiong, Z., Li, T., Algeo, T. J., & Dang, H. (2022). Sustained Deep Pacific Carbon Storage After the Mid-Pleistocene Transition Linked to Enhanced Southern Ocean Stratification. *Geophysical Research Letters*, 49(4). <https://doi.org/10.1029/2021GL097121>

Raymo, M. E., & Nisancioglu, K. H. (2003). The 41 kyr world: Milankovitch's other unsolved mystery. *Paleoceanography*, 18(1). <https://doi.org/10.1029/2002PA000791>

Raymo, M. E., Ruddiman, W. F., & Froelich, P. N. (1988). Influence of late cenozoic mountain building on ocean geochemical cycles. *Geology*, 16(7), 649. [https://doi.org/10.1130/0091-7613\(1988\)016<0649:iolcmb>2.3.co;2](https://doi.org/10.1130/0091-7613(1988)016<0649:iolcmb>2.3.co;2)

Roy, Martin, et al. "Geochemical Constraints on the Regolith Hypothesis for the Middle Pleistocene Transition." *Earth and Planetary Science Letters*, vol. 227, no. 3–4, Nov. 2004, pp. 281–96. *DOI.org (Crossref)*, <https://doi.org/10.1016/j.epsl.2004.09.001>.

Ruddiman, W. F., Raymo, M. E., Martinson, D. G., Clement, B. M., & Backman, J. (1989). *Stable isotope record, calcium carbonate concentrations, and sea surface temperature reconstructions of sediment cores from the North Atlantic* [Application/zip]. 10 datasets. <https://doi.org/10.1594/PANGAEA.701229>

Schaen, A. J., Jicha, B. R., Hodges, K. V., Vermeesch, P., Stelten, M. E., Mercer, C. M., Phillips, D., Rivera, T. A., Jourdan, F., Matchan, E. L., Hemming, S. R., Morgan, L. E., Kelley, S. P., Cassata, W. S., Heizler, M. T., Vasconcelos, P. M., Benowitz, J. A., Koppers, A. A. P., Mark, D. F., ... Singer, B. S. (2020). Interpreting and reporting $^{40}\text{Ar}/^{39}\text{Ar}$ geochronologic data. *GSA Bulletin*, 133(3–4), 461–487. <https://doi.org/10.1130/B35560.1>

Sexton, Philip F., and Stephen Barker. "Onset of 'Pacific-Style' Deep-Sea Sedimentary Carbonate Cycles at the Mid-Pleistocene Transition." *Earth and Planetary Science Letters*, vol. 321–322, Mar. 2012, pp. 81–94. *DOI.org (Crossref)*, <https://doi.org/10.1016/j.epsl.2011.12.043>.

Sosdian, S. M., et al. "Deep Atlantic Carbonate Ion and CaCO_3 Compensation During the Ice Ages." *Paleoceanography and Paleoclimatology*, vol. 33, no. 6, June 2018, pp. 546–62. *DOI.org (Crossref)*, <https://doi.org/10.1029/2017PA003312>.

Tabor, Clay R., and Christopher J. Poulsen. “Simulating the Mid-Pleistocene Transition through Regolith Removal.” *Earth and Planetary Science Letters*, vol. 434, Jan. 2016, pp. 231–40. *ScienceDirect*, <https://doi.org/10.1016/j.epsl.2015.11.034>.

Tachikawa, K., Rapuc, W., Dubois-Dauphin, Q., Guihou, A., & Skonieczny, C. (2020). Reconstruction of Ocean Circulation Based on Neodymium Isotopic Composition: Potential Limitations and Application to the Mid-Pleistocene Transition. *Oceanography*, 33(2). <https://doi.org/10.5670/oceanog.2020.205>

Watts, R. G., & Hayder, E. (1984). A two-dimensional, seasonal, energy balance climate model with continents and ice sheets: Testing the Milankovitch theory. *Tellus A*, 36A(2), 120–131. <https://doi.org/10.1111/j.1600-0870.1984.tb00232.x>

White, W. M. (2015). The K-Ar-Ca System. In *Isotope geochemistry* (1st ed.). chapter, Wiley/Blackwell.

Willeit, M., et al. “Mid-Pleistocene Transition in Glacial Cycles Explained by Declining CO₂ and Regolith Removal.” *Science Advances*, vol. 5, no. 4, Apr. 2019, p. eaav7337. *science.org (Atypon)*, <https://doi.org/10.1126/sciadv.aav7337>.

Wolff, E. W., et al. “Southern Ocean Sea-Ice Extent, Productivity and Iron Flux over the Past Eight Glacial Cycles.” *Nature*, vol. 440, no. 7083, Mar. 2006, pp. 491–96. *DOI.org (Crossref)*, <https://doi.org/10.1038/nature04614>.

Yehudai, M., Kim, J., Pena, L. D., Jaume-Seguí, M., Knudson, K. P., Bolge, L., Malinverno, A., Bickert, T., & Goldstein, S. L. (2021). Evidence for a northern hemispheric trigger of the 100,000-y glacial cyclicity. *Proceedings of the National Academy of Sciences*, 118(46). <https://doi.org/10.1073/pnas.2020260118>

